Understanding and control of compressively buckled semiconductor thin

films

Jihun Lima, Dejiu Fana, Byungjun Leea, and Stephen R. Forresta, b,c,1

^aDepartment of Electrical Engineering and Computer Science, University of Michigan,

Ann Arbor, MI 48109; ^bDepartment of Physics, University of Michigan, Ann Arbor, MI

48109; and Department of Materials Science and Engineering, University of Michigan,

Ann Arbor, MI 48109

¹ Stephen R. Forrest **Email:** stevefor@umich.edu

Keywords

Compressive buckling, Thin-walled beams, Compound semiconductors, Metamaterial,

Thermophotovoltaics, Infra-red reflectance

1

Abstract

We report the controllable buckling of free-standing thin film semiconductor metamaterials using a thin-walled structure spanning Au grid supports. The buckling is developed by compressing the Au grids, increasing the internal air pressure during the bonding of Au pads on the semiconductor to the grids, resulting in upward deformation. The stiffness of the free-standing semiconductor beam is controlled by the gridline spacing, as verified for a wide range of out-of-plane deformations, ranging from nearly flat to microns for gridline spacings from 20µm to 150µm, respectively. We also observe telephone-cord and domelike buckling as the gridline spacings and layer thicknesses are varied. Finite element analysis quantitatively predicts the shape and magnitude of the film deflection. We propose strategies to apply the distorted free-standing metamaterials for thermal energy harvesting, infrared reflectors, and pressure sensors.

Main Text

Introduction

Recent developments of advanced micro/nanomaterial applications such as optoelectronics, [1,2] bioelectronics, [3] wearable-electronics, [4] compressively buckled threedimensional (3D) mesostructures, [1,5-9] and metamaterials [10-15] demand device configurations that are inaccessible to conventional photolithographic processing. During the last decades, researchers have grafted stress-induced techniques onto existing 2D systems, providing promising routes to transform planar thin film surfaces and structures into 3D forms using pre-strained elastomeric substrates, [5-9] residual stress by thermal expansion coefficient mismatched materials, [16-18] and topological transformations. [19,20] Among them, thin films buckled by residual stresses have resulted in ribbons and wrinkled 3D mesostructures based on Si, [21-23] GaAs, [24-26] graphene, [27-29] and MoS₂. [17,30-32] The films with straight-sided, telephone-cord (TC),[33-35] and web-network patterns[17,31] have been developed using film delamination or blisters at the interfaces between substrates and films. A pre-strained soft substrate has enabled both upward and downward buckling in thin films. [36] However, these methods require relatively high temperatures, mismatches of thermal expansion coefficients, thereby limiting the range of available materials, accessible buckling dimensions, and shapes.

Here we present a method to compressively buckle free-standing group III-V alloy semiconductor thin films suspended between Au gridline supports. The demonstration resembles classical buckling formed by thermal residual stresses, blisters, or film delamination.^[16-18,33-35] In contrast to earlier work, however, the deformation of micron-scale structures results from a combination of a compressive, inward distortion of the Au

supports forming a cavity enclosed by the bridging thin film, and a thermally induced increase in air pressure within the cavity during bonding that pushes the film away from the substrate. The free-standing semiconductor structures are inspired by their recent use in air-bridge thermophotovoltaic (TPV) cells, where the air cavity between the thin film active region and a Au back reflector results in an extremely high reflectivity required for this application.^[37]

We show a wide range of buckling heights, ranging from nanometers to tens of microns. Finite element analysis (FEA) accurately predicts the morphology transformation from 2D-to-3D in the free-standing thin films. The micron-sized upward buckling is accurately modeled via classical Euler beam theory. [38,39] Using this theory, we explore a diversity of buckled metamaterials including nearly flat, extreme upward buckling, TC buckling, and dome-like buckling. The fabrication process is compatible with conventional 2D lithography and produces a range of controllable morphologies useful for the formation of precisely shaped metasurfaces required in airgap devices for energy harvesting, optics, and sensing.

Results and Discussion

Figure 1 illustrates the steps for fabrication of buckled structures on free-standing films suspended between Au grids. A crystalline semiconductor multilayer (ML) thin film is comprised of epitaxial 0.2 μm InGaAs (Be-doped, 1×10¹⁸ cm⁻³)/0.1 μm InP (Be-doped, 1×10¹⁸ cm⁻³)/1.0 μm InGaAs (Si-doped, 1×10¹⁷ cm⁻³)/0.1 μm InP (Si-doped, 1×10¹⁸ cm⁻³)/0.1 μm InGaAs (Si-doped, 1×10¹⁸ cm⁻³) grown by solid-source molecular-beam-epitaxy (MBE) on a (100) p-type InP substrate. Step 1: The 500 nm-thick Au grids with 100 μm

spacings are photolithographically patterned onto the epitaxial layer surface. A 2D beam structure is defined across the gridlines, where the free-standing membrane (the "beam") spans the grids (the "beam supports"). Step 2: To transfer the epilayers from the InP substrate to a Si substrate precoated with Au, the facing surfaces are pressure-bonded to form a metal-metal weld at 150°C in air (Step 3: see Materials and Methods). [37,40,41] Step 4: After bonding, the InP substrate is removed by selective wet etching, resulting in thin-walled cavities enclosed by the Si, the membrane, and the supports. Step 5: The bonding force compresses the Au grids, distorting them into the cavities. This offers an opportunity to apply lateral loading to the free-standing film. The force reduces the volume, causing the internal air pressure (P_i) to increase, thus forcing the beam upward, away from the substrate. The supports remain deformed, and P_i is higher than the initial air pressure (P_{init}) ≈ 0.101 MPa). As a result, it generates parallel compressive strains at the bottom surface of the film. On the other hand, when the empty spaces are evacuated, P_i is lower than P_{init} , and the film flexes downward.

Once the cavity is evacuated, it is compressed during the bonding step. The bottom surface of the epilayer is then tensile stressed – here the compressive stress direction is normal to the tensile stress. Thus, control of the initial internal pressure determines whether the buckled morphology is upward or downward. Although the semiconductor and the Au films have different thermal expansion coefficients (InP and InGaAs: 4.60-5.66×10⁻⁶/K, Au: 14×10⁻⁶/K), the bonding temperature is sufficiently low that the residual thermal stress is negligible at the Au-Au bonding interface and at the interface between the semiconductor and the Au films. During the bonding phase, the air cavity is heated to 150°C, and its

volume expands. Since the materials surrounding the cavity are stiff, the volume expansion is small and is released upon cooling. Nevertheless, the Au grids remain slightly distorted. This results in a residual elevated pressure that results in the buckled morphology.

The microscope image in Fig. 2A shows a 1 mm diameter circle with multiple Au gridlines supporting the upwardly buckled free-standing film. The longitudinal grid lengths in the y-direction vary from left to right, whereas in the x-direction, the 100 μ m gap between the supports is constant, except in the boundary regions of the circle that determine the beam length. The thin-walled beam structure extends to the periphery of the circle. The buckling shapes and sizes of the membrane are determined by the 100 μ m gaps.

From classical Euler beam theory,^[42,43] the upward buckling is achieved by axial force loading of the beam when a critical loading force (P_{cr}) and a stress (σ_{cr}) are less than the yield strength (σ_y) of the free-standing material. During bonding, the distortion of the grid results in P_{cr} lateral to the film. Then compressive buckling follows:

$$\frac{P_{cr}}{A} = \sigma_{cr} = \frac{\pi^2 E_t I}{A(l_t)^2} = \frac{\pi^2 E_t}{(l_t/r)^2} < \sigma_y, \tag{1}$$

where A is the beam cross-sectional area in the buckling direction (x-axis in Fig. 2A), E_t is its Young's modulus, l_t is the effective beam length, I is the area moment of inertia of the beam cross section, and $r = h_t/\sqrt{12}$ is the radius of gyration for a rectangular beam of thickness (h_t). The slenderness ratio is l_t/r . The beam length along the x-axis is $l_{tx} = 100$ µm, whereas the lengths in the y-axis (l_{ty}) are longer than l_{tx} although they differ through the buckling regions. The slenderness ratios range from 230 to 2300, where σ_{cr} , $<\sigma_{y} \sim 100$ GPa for the InP/InGaAs film (see Supporting Information, SI). [44]

Figure 2B shows a FEA simulation of the experimental compressive strain distribution in the thin film during bonding (see SI, Fig. S1 for modeling methods). The strain in the film at the grid lines is approximately zero, whereas non-zero compressive strain appears in the free-standing film.

The Young's modulus (E_y) and hardness of the InGaAs, epitaxial layers, and Au films are extracted by nanoindentation employing a 50-200 nm radius diamond tip on a three-sided pyramid Berkovich probe (see SI, Fig. S2). In Table 1, the difference in E_y between Au and semiconductor films is $\sim 10\%$, but the Au hardness is noticeably lower than that of the semiconductor, resulting in a larger Au grid deformation. To characterize the deformation, microindentation measurements were performed using a 50 μ m radius spherical probe tip, with results in Fig. 2C. Due to its higher hardness, the semiconductor membrane endures large loading forces without significant plastic deformation relative to the Au film. This allows structural deformation of III-V materials that follows the Au surface shape. The same microindentation was performed in the distorted region. The loading and unloading curves overlap and exhibit a linear relationship between the displacement and the loading force. The maximum indentation depth is 3.8 μ m at 3.4kN. Once a buckled morphology is formed, it is elastic and rapidly responds to external forces while maintaining its mechanical stability.

To investigate the dependence of the grid distortion on pressure, we traced the grid profiles before and after transferring the gridlines onto a Au-coated Si substrate using laser confocal microscopy (Fig. 2D). The grid height was compressed by approximately 1.6% and the grid width was extended by 3.5%.

$$h_b(x) = A \times exp(-\frac{1}{2}((x - x_c)/w)^2),$$
 (2)

where $h_b(x)$ is the buckling height, A is the amplitude of the distortion, x_c is the peak center, and w is its width.

Figure 3 shows a set of experimental buckled, 0.5 mm diameter circles with different grid spacings. The three-dimensional FEA simulations accurately predict local pop-up buckling of the free-standing films resulting from the residual stress from the Augrid deformation. Details of the simulation methods are provided in the Supporting Information (see SI Note 3, and Fig. S3). The FEA simulations also predict the upper and lower bounds of the strains in the buckling with two boundary conditions: one is the Augridline deformation, and the other is the internal pressure in the air cavity. Further definitions of variables that characterize the film profile are found in the inset of Fig. 4A. Due to the uncertainty of the quantitative analysis of the pressure-density relation and Gauss' theorem in the air cavity, [45] the internal pressures are numerically estimated to fit the simulated buckling heights to experiment in Fig. 4A.

The FEA Case-1 corresponds to buckling without structural distortion of the Au grids. The internal pressures are appropriately adjusted to match the buckling heights (h_b) equivalent to the measurements. From the results, the black-dotted line gives the strains in the buckled III-V thin films (see SI Note 3, and Fig. S3). The strain increases with increasing spacing, and then decreases when the spacing is larger than $100\mu m$. As expected, the effect of the internal pressure caused by Au deformation weakens as the cavity volume increases.

Case-2 assumes the Au grids are distorted by the 70N compression force. The buckling heights and strains are comparable to those in Case-1 for forces < 70N. On the other hand, Case-3 includes the plastic deformation of the Au-gridlines by the welding

force (2 kN) applied in the normal direction. At gridline spacings < 70 μ m, the calculated buckling heights are larger than experiment even though the internal pressures are set to zero. Additionally, by reducing the grid spacing, the strain (red-triangle-dotted line) is significantly higher than Case-1 or 2. This implies that the variations of the strain and height are more strongly affected by Au deformation at relatively small grid-spacings. Interestingly, at a relatively large grid spacing, the simulated strains are not significantly different in the three cases. The Au distortion generated by a given loading force is inversely proportional to contact area. That is, the upper and lower bounds of the strains rely on the cavity spacing, the grid designs, and the mechanical properties of the materials used. The experimental strains (red filled circles) are determined using profilometry, where the initial lengths of x_0 are adjusted to fit the lower bound line (see SI Note 1). Fits, fitting parameters, and FEA simulation methods are found in Fig. S4, Table S1, Note 4 in SI for several grid spacings.

From these results, the buckling height and strain (ε_b) are functions of gridline spacing. The stiffness of the structure is proportional to E_tI/I^3 . For example, the gridline spacing only varies from 20 μ m to 150 μ m by 7.5 times, but the stiffness is dynamically changed by $7.5^3 \approx 422$. Therefore, the buckling height maximum, h_b , increases from 10 nm for a grid spacing of 20 μ m, to 4.5 μ m for a spacing of 150 μ m. Remarkably, the buckling height at the same gridline spacing is unaffected by the circle diameter (see SI, Fig. S5 and Fig. S6) when it is greater than the spacing. While the fracture limit of the semiconductor is $1\sim2\%$, the strains are $\varepsilon_b<0.3\%$. Hence, the buckling process is non-destructive to the suspended film. The buckling patterns show a controllable range from nanometers to

microns, depending on the grid structures, materials, and the fracture limit of the membrane.

Figure 4B shows x-ray diffraction (XRD) patterns of the as-grown epitaxial film and the buckled metamaterial. The left and right peaks correspond to the InGaAs and the InP layers, respectively, with a lattice-mismatch of 0.4%. However, the critical thickness $(h_c = a_{epi}/2f \text{ where } a_{epi} = \text{lattice constant of an epilayer, and } f = \text{lattice mismatch})$ to relax the elastic strain energy accumulated in the epitaxial layer, particularly close to the interface, is ~ 70 nm. This is smaller than the total layer thickness, indicating that the lattice-mismatched layers are relatively free of defects. The diffraction peaks in the buckled sample are shifted to a larger half angle, θ , for the buckled film, indicating compressive strain (see Table 2). At the InGaAs peak center, the shift is $\Delta(2\theta) = 0.117 \pm 0.003^{\circ}$, corresponding to a compressive strain of $0.1664 \pm 0.0047\%$.

After loading, the curvature is determined by the buckling mode. The effective beam lengths are approximately 50% to 70% of the gridline spacings (W_g) (see Table S2), consistent with the Euler's assumption for a beam fixed at the Au grid supports. In Fig. 5A, film thicknesses from 1.5 μ m to 3.9 μ m result in buckling heights from 2.5 μ m to 30 nm, respectively. FEA predicts that a 5 μ m-thick epilayer achieves nearly zero deflection at the same grid spacing. The TC morphology at the buckling mode transition is achieved at 0.7 μ m, arising from geometric imperfections in the grids. [46-48] In contrast, thicker layers are undisturbed by imperfections in the thin-walled beam structures. The FEA accurately predicts the sinusoidal buckling peak positions in the free-standing film, as shown to the left of Fig. 5A.

Figure 5B-D compare the buckling attained by removing the gridlines within the circles. In Fig. 5B, the film thickness is 3.9 μm, resulting in a uniform dome shape. The air volume expansion depends on the pressure applied during cold-welding and the film thickness (see also SI, Fig. S7). Figure 5C-D show the buckling mode transition when the film thickness is decreased to 0.7 μm. The dome is transformed into four and eight segmented circles whose peak positions are accurately predicted by FEA. The resulting mesostructures show geometrical complexity that offer opportunities to access a diversity of 3D shapes. On the other hand, the zero-deflection free-standing microstructures can enable high reflectivity air-bridge III-V photovoltaics^[37] in near-field radiative heat transfer applications.^[49,50] Additionally, since the microstructures are elastic, they provide a platform for sensitive pressure sensors and optical elements.^[51,52]

Conclusions

In summary, we have presented a comprehensive study of the compressive buckling of free-standing semiconductor thin films that controllably transforms flat inorganic microstructures into scalable, buckled metamaterials. The study applies classical Euler's beam theory where the thin inorganic semiconductor membrane constitutes a beam suspended between Au gridline supports. The accuracy of this approach is confirmed by experiment and finite element analysis that quantitatively predicts the scale and shape of the deformation as a function of material elastic properties, beam length, thickness and loading conditions. The strain is smaller than the elastic limits of inorganic materials, and hence does not result in fracture of the brittle, crystalline inorganic thin films, and yet is large enough to achieve a wide range of deflections from nanometers to tens of microns.

The distortion is eliminated as the film thickness is increased to approximately 5% of the span length. A flat surface is required in applications such as in high efficiency near-field photovoltaic heat transfer.^[50] In contrast, the buckled semiconductor linearly responds to an external force, offering applications in sensitive pressure sensors in electronic skins, medical devices, and wearable devices, as well as in deformable optical elements.

The results presented can readily be extended to different beam and grid line materials. Using the known mechanical properties of a free-standing thin film membrane and the beams are inserted into our models, we can accurately predict the extent to which the metamaterial is distorted, and the robustness of the free-standing layer. While we have only demonstrated the three-dimensional structures comprising an elastic beam spanning thin Au gridlines, the results deliver a means to explore a broad range of structures on mixed materials platforms with different designs. The controllable buckling of metamaterials has potential for creating precisely designed mesostructures and metasurfaces.

Materials and Methods

Fabrication of mesostructures. The Si substrate is treated in a buffered hydrofluoric (BHF) acid solution to remove its native oxide. It is ultrasonically cleaned in acetone, isopropyl alcohol, and de-ionized water, and then dried in a stream of N₂ gas. A 30nm Ti/500nm Au contact layer is deposited by e-beam evaporation on the pre-cleaned Si wafer. The epitaxial films are grown on the (100) surface of an InP wafer by solid source molecular beam epitaxy. The 500 nm thick Au gridlines are deposited on the epilayer using electron-beam evaporation, and patterned using a conventional lift-off process. To bond the Au on the epilayer to that on the Si substrate, the wafers are brought into contact, and the sandwich is loaded into a wafer bonder chamber (EVG 510 and EVG 520, EV Group Inc., Tempe, AZ, USA) in air. The vacuum gap is applied in the bonding chamber before applying the uniaxial bonding force to the sample. A bonding pressure of 10 MPa (20N/sec ramping rate) is applied at the top of the InP wafer at 150 °C for 5 min, and subsequently the sample is cooled to room temperature. The InP substrate is etched away by immersion in dilute hydrofluoric acid (HCl) (1:1) for 8 h.

Finite-Element-Analysis for 3D buckled structures. Post-buckling analyses were supported by finite-element-analysis (FEA) using COMSOL Multiphysics, v.5.5. A physics option for solid mechanics (Solid Mechanics) is used to calculate the structural deformation. To simulate the strain distributions during cold welding in three dimensions, we assume that the bonding force is applied in the z (i.e., normal)-direction. The initial air pressure in the cavity as 0.101 MPa (1 atm). The bonding force increases the internal pressure to 1 MPa, which is adjusted to fit the measured buckling heights. A uniaxial force of 2000 N is applied to the Au gridlines along z. The displacement of the bottom boundary

of the modeled structure is constrained, which is the same as in the experiment. We used experimentally extracted mechanical parameters for InGaAs, multilayers, and Au materials provided in Table 1.

Buckling measurements. Non-contact optical 3D profilers were used to characterize the buckling shapes, (Zygo NewView 5000, Zygo Corporation, Middlefield, CT, USA, and Olympus OLS 4000 LEXT, Olympus Corporation, Tokyo, Japan). Profilometer line-scans were performed by a diamond-tip stylus tool (BRUKER, Dektak XT, Bremen, Germany) with a minimum force of 9.8 μN. Nanoindentations were carried out by a Hysitron Ti 950 Tribo-indenter with a Berkovich sharp diamond-tip to measure E_y and hardness. A spherical indenter (50 μm 90° conical probe) was used to measure inelastic deformations on planar and buckled surfaces. Film crystallinity was determined using the Cu Kα 1.5418 Å radiation at 40 kV and 44 mA using a Smartlab diffractometer (Rigaku Corporation, Tokyo, Japan).

Au gridline deformation measurements. A confocal laser optical profilometer (LEXT OLS 4000, Olympus, Tokyo, Japan) was used to measure the profiles of the Au gridlines before and after transfer onto a Au-coated Si substrate. The 500nm thick Au gridlines are formed on a precleaned InP substrate using lift-off. The grids were transferred to the Si substrate by cold welding (10MPa at 150°C in air during 5min). After removing the InP substrate, the grid profile at the same position was also measured.

Acknowledgements

The authors would like to acknowledge the Michigan Center for Materials Characterization at the University of Michigan for the use of the nanoindentation instrument and staff assistance. The authors also acknowledge Profs. M. Thouless and P. Reddy, and Mr. R. Mittapally for helpful discussions. We thank the University of Michigan's XMAL for its assistance with the Rigaku Smartlab XRD. Structure fabrication was performed at the Lurie Nanofabrication Facility at the University of Michigan. This research was sponsored by the Army Research Office (ARO) under Grant Number W911NF-18-1-0004. The views and conclusions contained in this document are those of the authors and should not be interpreted as representing the official policies, either expressed or implied, of the ARO or the U.S. Government. The U.S. Government is authorized to reproduce and distribute reprints for Government purposes notwithstanding any copyright notation herein.

References

- [1] M. Schumann, T. Buckmann, N. Gruhler, M. Wegener, and W. Pernice, Light-Science & Applications 3, e175 (2014).
- [2] D. Yin, J. Feng, R. Ma, Y. Liu, Y. Zhang, X. Zhang, Y. Bi, Q. Chen, and H. Sun, Nature Communications 7, 11573 (2016).
- [3] C. Zhang, H. Deng, Y. Xie, J. Su, and J. Lin, Small 15, 1904224 (2019).
- [4] Y. Ling et al., Acs Nano 12, 12456 (2018).
- [5] H. Fu *et al.*, Nature Materials **17**, 268 (2018).
- [6] K. Bai et al., Science Advances 6, eabb7417 (2020).
- [7] Y. Sun, W. Choi, H. Jiang, Y. Huang, and J. Rogers, Nature Nanotechnology 1, 201 (2006).
- [8] H. Zhao *et al.*, Proceedings of the National Academy of Sciences of the United States of America **116**, 13239 (2019).
- [9] S. Xu et al., Science **347**, 154 (2015).
- [10] P. Wang, F. Casadei, S. Shan, J. Weaver, and K. Bertoldi, Physical Review Letters 113, 014301 (2014).
- [11] J. Paulose, A. Meeussen, and V. Vitelli, Proceedings of the National Academy of Sciences of the United States of America **112**, 7639 (2015).
- [12] E. Filipov, T. Tachi, and G. Paulino, Proceedings of the National Academy of Sciences of the United States of America **112**, 12321 (2015).
- [13] V. Shalaev, Nature Photonics 1, 41 (2007).
- [14] T. Frenzel, M. Kadic, and M. Wegener, Science **358**, 1072 (2017).

- [15] X. Ni, Z. Wong, M. Mrejen, Y. Wang, and X. Zhang, Science **349**, 1310 (2015).
- [16] J. Hutchinson, M. Thouless, and E. Liniger, Acta Metallurgica Et Materialia 40,295 (1992).
- [17] H. Ren et al., Acs Nano 13, 3106 (2019).
- [18] Y. Shi, A. Bork, S. Schweiger, and J. Rupp, Nature Materials **14**, 721 (2015).
- [19] R. Jackman, S. Brittain, A. Adams, M. Prentiss, and G. Whitesides, Science 280, 2089 (1998).
- [20] D. Fan, B. Lee, C. Coburn, and S. Forrest, Proceedings of the National Academy of Sciences of the United States of America **116**, 3968 (2019).
- [21] Q. Zhang, Y. Tang, M. Hajfathalian, C. Chen, K. Turner, D. Dikin, G. Lin, and J. Yin, Acs Applied Materials & Interfaces **9**, 44938 (2017).
- [22] C. Yu, Z. Wang, H. Yu, and H. Jiang, Applied Physics Letters 95, 141912 (2009).
- [23] H. Jiang, D. Khang, J. Song, Y. Sun, Y. Huang, and J. Rogers, Proceedings of the National Academy of Sciences of the United States of America **104**, 15607 (2007).
- [24] Y. Sun, V. Kumar, I. Adesida, and J. Rogers, Advanced Materials 18, 2857 (2006).
- [25] A. Shevyrin *et al.*, Applied Physics Letters **101**, 241916 (2012).
- [26] H. Jiang, Y. Sun, J. Rogers, and Y. Huang, Applied Physics Letters 90, 133119 (2007).
- [27] T. Jiang, R. Huang, and Y. Zhu, Advanced Functional Materials 24, 396 (2014).
- [28] H. Hattab *et al.*, Nano Letters **12**, 678 (2012).
- [29] W. Lee, J. Kang, K. Chen, C. Engel, W. Jung, D. Rhee, M. Hersam, and T. Odom, Nano Letters **16**, 7121 (2016).
- [30] A. Azcatl *et al.*, Nano Letters **16**, 5437 (2016).

- [31] S. Kim, D. Kim, J. Lim, S. Cho, S. Kim, and H. Jung, Acs Applied Materials & Interfaces 8, 13512 (2016).
- [32] H. Ren, L. Zhang, and G. Xiang, Applied Physics Letters 116 (2020).
- [33] M. Thouless, Journal of the American Ceramic Society **76**, 2936 (1993).
- [34] J. Faou, G. Parry, S. Grachev, and E. Barthel, Physical Review Letters **108**, 116102 (2012).
- [35] Y. Ni, S. Yu, H. Jiang, and L. He, Nature Communications 8, 14138 (2017).
- [36] Y. Zhang, F. Wang, Y. Ma, and X. Feng, International Journal of Solids and Structures **161**, 55 (2019).
- [37] D. Fan, T. Burger, S. McSherry, B. Lee, A. Lenert, and S. Forrest, Nature **586**, 237 (2020).
- [38] O. A. Bauchau and J. I. Craig, *Structural analysis : with applications to aerospace structures* (Springer, Dordrecht; New York, 2009), Solid mechanics and its applications,, 163.
- [39] A. Sears and R. Batra, Physical Review B **73**, 085410 (2006).
- [40] K. Lee, J. Zimmerman, T. Hughes, and S. Forrest, Advanced Functional Materials **24**, 4284 (2014).
- [41] D. Fan, K. Lee, and S. Forres, Acs Photonics 3, 670 (2016).
- [42] G. Wang and X. Feng, Applied Physics Letters **94**, 141913 (2009).
- [43] H. Yap, R. Lakes, and R. Carpick, Nano Letters 7, 1149 (2007).
- [44] G. Patriarche and E. Le Bourhis, Journal of Materials Science Letters **20**, 43 (2001).
- [45] W. Duschek, R. Kleinerahm, and W. Wagner, Journal of Chemical Thermodynamics 22, 841 (1990).

- [46] B. Schafer and T. Pekoz, Journal of Constructional Steel Research 47, 193 (1998).
- [47] Z. Kolakowski, T. Kubiak, M. Zaczynska, and F. Kazmierczyk, International Journal of Mechanical Sciences **184**, 105723 (2020).
- [48] M. Deml and W. Wunderlich, Computer Methods in Applied Mechanics and Engineering **149**, 201 (1997).
- [49] A. Fiorino, L. Zhu, D. Thompson, R. Mittapally, P. Reddy, and E. Meyhofer, Nature Nanotechnology **13**, 806 (2018).
- [50] R. Mittapally, B. Lee, L. Zhu, A. Reihani, J. Lim, D. Fan, S. Forrest, P. Reddy, and E. Meyhofer, Nature Communications **12**, 4364 (2021).
- [51] S. Mannsfeld, B. Tee, R. Stoltenberg, C. Chen, S. Barman, B. Muir, A. Sokolov, C. Reese, and Z. Bao, Nature Materials **9**, 859 (2010).
- [52] Y. Zang, F. Zhang, D. Huang, X. Gao, C. Di, and D. Zhu, Nature Communications 6, 6269 (2015).

Table 1. Extraction of mechanical properties by nanoindentation.

Material	$E_r(GPa)$	Hardness (GPa)	E_y (GPa)	Poisson's ratio (ν)
InGaAs	104.01	9.8	101.94	0.33
Au	102.4	1.84	90.68	0.44
III-V multilayers	90.61	6.39	87.68	0.33

Table 2. XRD measurements on the as-grown and buckled thin films.

Samples	Materials	2θ (deg)	Full width at half maximum
As-grown films	InGaAs	62.96	0.093
2.20 8.0	InP	63.27	0.046
Buckled metamaterial	InGaAs	63.08	0.098
	InP	63.38	0.134

Figure captions

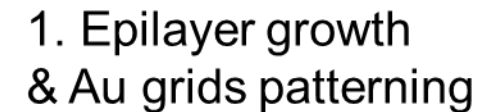
Figure 1. Schematic of the fabrication process. (1) The epitaxial layer with Au-gridlines is grown by molecular beam epitaxial growth, e-beam deposition of the Au film, and conventional photolithography. (2) The epitaxial layer is bonded onto a Si substrate, also coated with Au, by cold welding. (3) The thick substrate stabilizes the epitaxial film during bonding. The pressure of air or vacuum in the space between the Au gridlines determines the deformed shape of the film, and thus the direction of the compressive strain through the bottom surface of the epilayer. (4)-(5) After removal of the substrate, the Au deformation generates the buckled morphology.

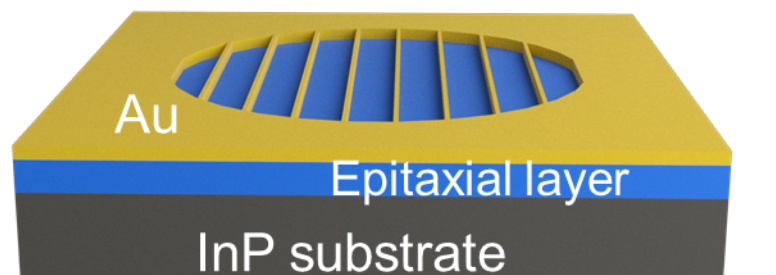
Figure 2. Buckle generation by compressive strains and stresses. (A) Optical microscope image of the buckled sample with the gridline spacing of 100 μm. Scale bar, 200 μm. (B) Simulations of the compressive strain distribution in the film. Scale bar, 200 μm. (C) Load-displacement curves of III-V multilayer (ML), Au, III-V ML on Au, and buckling using a spherical indenter. (D) Profiles of the Au gridline before and after compression. The top images are observed by a laser confocal microscope at the same position. The scale bar is 40 μm. The bottom graph is the profilometry results.

Figure 3. Scalable semiconductor microstructures and strains. 2D and 3D optical images, and FEA simulations of the compressively buckled mesostructures with different Au gridline spacing. Scale bars, $100 \mu m$. The legends indicate the displacements. The exp erimental buckling heights are in the SI, Fig. S5.

Figure 4. Strains in the buckled semiconductors. (*A*) Buckling heights and numerically estimated strains. The simulations show three cases – there is no Au deformation in Case-1, and Cases-2 and -3 assume that the Au gridlines are plastically deformed by the compression forces of 70 N and 2 kN, respectively. Inset: Illustration of the buckled film defining variables used in text. (*B*) X-ray diffraction (XRD) patterns on the as-grown vs. t he buckled metamaterial. The black curve is the XRD pattern of the as-grown thin film, the blue curve is the XRD pattern of the buckled film.

Figure 5. Film thickness dependence. (*A*) Optical microscope images of buckling morphologies for various film thicknesses. The Au gridline spacing is 100 μm in the 0.5 mm and 1 mm circles. The buckling transitions to a telephone cord (TC) morphology at 0.7 μm. Scale bars, 200 μm. FEA accurately predicts the post buckling peak positions for TC buckling. (*B*) Buckling in 600 μm diameter circles for a film thickness of 2.7 μm. Scale bar, 100 μm. The right-top image was measured by a laser confocal microscope, the bottom indicates the FEA result. Geometrically segmented buckling for (C) 500 and (D) 300 μm diameter circles. Scale bars, 100 μm. The FEA results accurately predict the buckling peak positions.





2. Au-Au bonding by cold welding

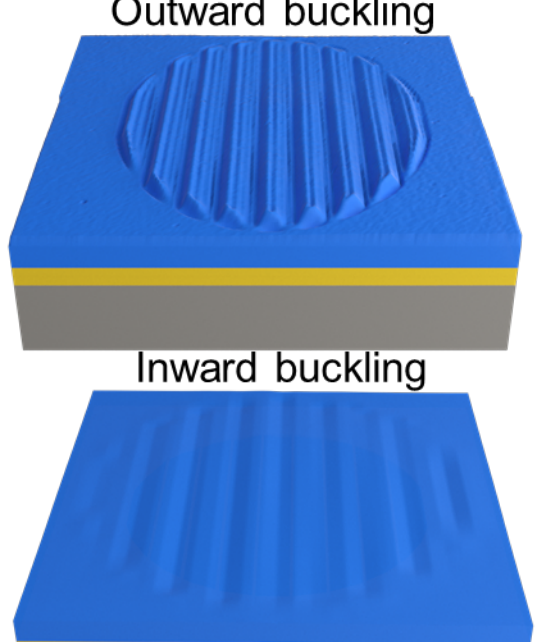
InP substrate

Si substrate

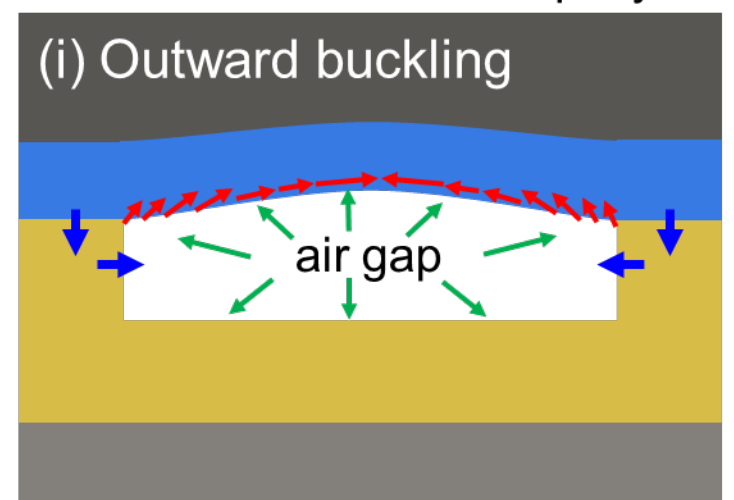
→ 4. Buffer substrate removal

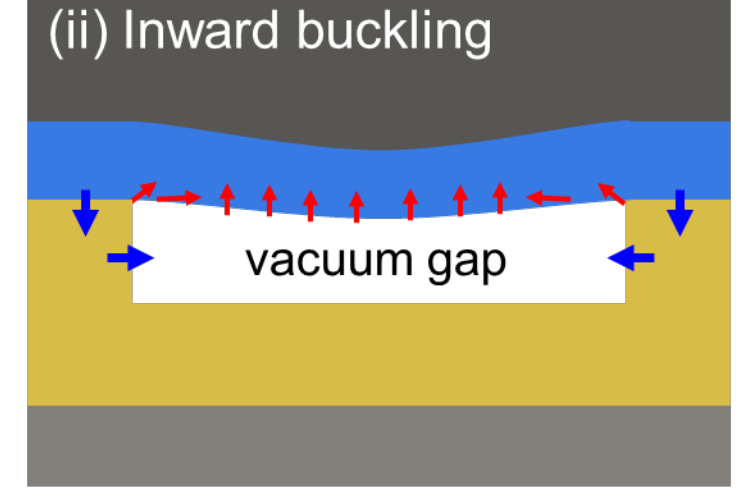


Buckling generationOutward buckling

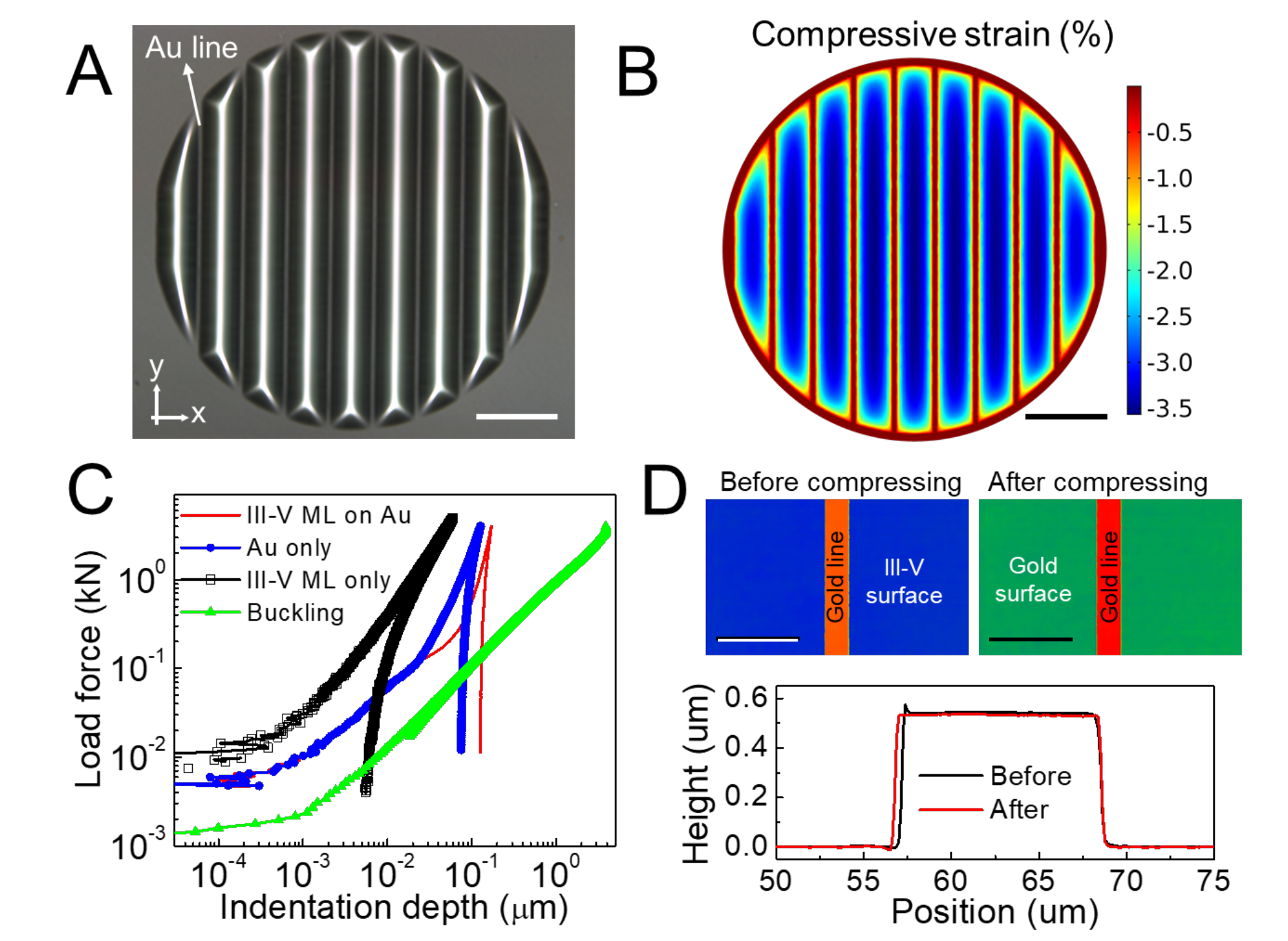


3. Compressive strain direction at the bottom surface in the epilayer





- → Compressive strain direction
- → Au grid deformations
- → Internal pressure



Grid spacing	2D images	3D images	FEA
20μm			10 µm 8 ×10 ⁻³ 6 4 2 0
50μm			0.5 μm 0.4 0.3 0.2 0.1 0.0
100µm			2.5 µm 2.0 1.5 1.0 0.5 0.0
150µm			4.0 µm 3.0 2.0 1.0 0.0

